

Article

# Retrieval and Analysis of the Strongest Mixed Layer in the Troposphere

Zheng Sheng <sup>1</sup>, Lesong Zhou <sup>1,\*</sup> and Yang He <sup>1</sup>

College of Meteorology and Oceanography, National University of Defense Technology, Changsha 410073, China; 19994035@sina.com (Z.S.); heyang12357@sina.com (Y.H.)

\* Correspondence: 17327729696@163.com; Tel.: +86-199-7299-4996

Received: 2 December 2019; Accepted: 4 March 2020; Published: 6 March 2020



**Abstract:** In this article, Thorpe analysis, which often retrieves the characteristics of mixing in the free atmosphere from balloon sounding data, is applied to the data of the Constellation Observing System for Meteorology, Ionosphere and Climate (COSMIC). We find that the COSMIC data can well retrieve the strongest mixed layer in the troposphere (SMLT) altitude, and can reveal the basic variation trend of the SMLT thickness and Thorpe scale  $L_T$ . We use COSMIC data to reveal the global spatial and temporal distribution of the SMLT from 2007 to 2015 and analyze the fluctuation period of the SMLT altitude with Hilbert–Huang transform (HHT), we find that the variation of the SMLT altitude is influenced by the dual effects of terrain and solar radiation.

**Keywords:** turbulence; strongest mixed layer; troposphere; Thorpe analysis

## 1. Introduction

Atmospheric turbulence is an important research subject in the field of Atmospheric Science. It is of great importance in understanding the energy budget and momentum transfer in the atmosphere [1,2]. However, as the turbulence of the free atmosphere is episodic and complex, and the detection of the free atmosphere is limited by the quality (altitude and resolution) [3–5], the study of the atmospheric turbulence in the free layer is still relatively undeveloped. Due to the lack of understanding of the turbulence in the free atmosphere, we are unable to grasp its changing laws, which has severely affected the flight safety of aircraft in the free atmosphere and limited the skill of NWP (Numerical Weather Prediction) and climate models [6–9]. Among the existing means, in situ measurements using turbulence probes on research aircraft are both costly and few in number [10,11]. Radar probing using Doppler radars is more convenient but often subject to uncertainties [12,13]. In order to retrieve the characteristics of turbulence of free atmosphere from balloon sounding data, Thorpe analysis, which was originally applied to the study of ocean mixing [14,15], has been used by many references to analyze balloon sounding data [16–20]. This innovative method provides an alternative approach to the study of free atmospheric turbulence. The Thorpe analysis is a method to obtain the turbulence parameters by calculating the difference between the detected potential temperature profile or potential density profile and the reference profile obtained by sorting the data in ascending order [14,15]. In the free atmosphere, with the use of balloon radiosonde to detect the temperature, pressure and humidity, we can get the potential temperature ( $\theta$ ) profile. However, the profile is unstable and it contains a lot of inversions, namely some areas where larger  $\theta$  is in the lower layer, and smaller  $\theta$  is in the higher layer. In order to obtain a stable profile, the  $\theta$  will be arranged in an ascending order. In this process, supposing that  $\theta_m$  at  $z_m$  needs to be moved to  $z_n$  after rearrangement ( $m$  and  $n$  represent the sequence

number of this data in the dataset), then the Thorpe displacement will be  $D = z_n - z_m$ . The root mean square of all  $D$  in the entire inversion is the Thorpe scale,

$$L_T = \sqrt{\frac{\sum_{i=1}^N D_i^2}{N}} \quad (1)$$

which characterizes the scale of the inversion.  $L_T$  is related to the Ozmidov scale  $L_O$ , which is an important scale to describe turbulence characteristics, is represented by

$$L_O = c L_T \quad (2)$$

where  $c$  is empirical constant,  $L_O = \left(\frac{\varepsilon}{N^3}\right)^{\frac{1}{2}}$ ,  $\varepsilon$  is the turbulent energy dissipation rate and  $N$  is the buoyancy frequency. In recent years, some related studies have been published. In these studies, Thorpe analysis was applied to sounding data in different regions of the earth. In 2010, Nath et al. [17] made statistics on the vertical distribution characteristics of turbulence over Gadanki sounding station for three years through the Thorpe analysis and found that from the troposphere to the low stratosphere, the  $\varepsilon$  increase from  $10^{-7}$  to  $10^{-3}$   $\text{m}^2/\text{s}^3$ ; In the same year, Kantha and Hocking [18] used the Thorpe analysis to compare balloon detection results with radar detection results for four consecutive months, and found that the two have good consistency. In 2011, Wilson et al. [20] compared the detection ability of conventional resolution radiosonde and high-resolution radiosonde to turbulence in free atmosphere by the Thorpe analysis, and proposed that if the noise is strictly controlled, the data of conventional radiosonde can be used to analyze the climate characteristics of turbulence. In 2016, Muhsin et al. [20] studied the turbulence characteristics over two tropical sounding stations in India by the Thorpe analysis, and found that the turbulence intensity and atmospheric stability within 3–10 km have obvious diurnal changes, but there is no obvious diurnal change over 15 km. These researches contribute to the knowledge of the turbulence of free atmosphere.

The traditional balloon sounding method has many advantages, such as the high accuracy and resolution of detection; some sounding stations can accumulate sounding data of many years by releasing sounding balloons every day. That is why the Thorpe analysis is often used to analyze balloon sounding data. However, for balloon sounding, only a small range of detection data obtained over the station without a global observation means the global turbulence characteristics can't be obtained. At the same time, satellite observations can carry out long-term global observation, but the accuracy and resolution of the observation are far less than the balloon sounding data, so it seems difficult to apply the Thorpe analysis to satellite observation data. However, some researchers' studies show that there was a larger  $L_T$  stratification in the middle of the troposphere, and its  $L_T$  value could reach over one hundred or even hundreds of meters [17,20–22]. The value of  $D$  is also large enough to be within the resolution of some satellite detection data. However, no research to-date has used the Thorpe technique on satellite data to research this layer. So, we call this layer of atmosphere the strongest mixed layer of the troposphere (SMLT), and try to use satellite observation data to discover the global spatial and temporal distribution of this layer of the atmosphere.

The satellite data used in this article are COSMIC radio occultation data. COSMIC is a cooperative project of several agencies in Taiwan and the United States. It was launched in April 2006 to carry out GNSS (global navigation satellite system) occultation tests [23]. The entire COSMIC system consists of 6 LEO (low-Earth-orbit) satellites weighing about 62 kg, revolving around the earth and receiving signals from 24 United States global positioning satellite GPS (global positioning system) [24]. The refraction of atmosphere will cause the bending of the radiowave path. The ground analysis center obtains the bending angle of the GNSS signal on the atmospheric path according to the geometrical optics principle, and then the refractive index of the atmosphere can be obtained. Finally, combining the refractive index and one dimensional variational method, we can get the global atmospheric

temperature, pressure, humidity and ionospheric profile [25,26]. After obtaining this data, we can use the Thorpe analysis to retrieve SMLT's physical characteristics (altitude, thickness and  $L_T$ ).

In order to further study the change characteristics of the physical properties of SMLT with time, we use the Hilbert–Huang transform (HHT) to extract the main mode and fluctuation period of SMLT altitude varying with time. HHT is a time series analysis method proposed by Huang and other scholars in 1998 [27]. HHT includes two parts: the empirical mode decomposition (EMD) and Hilbert transformation. The core of EMD is to decompose the signal into a series of intrinsic mode functions (IMFs) from high frequency to low frequency based on its time scale characteristics. However, EMD has the problem of mode mixing, that is to say, the similar time scales may be distributed in different IMF. In order to solve this problem, Wu et al. [28] put forward the ensemble empirical mode decomposition (EEMD) method. EEMD introduces white noise and makes ensemble averaging to avoid the mode mixing problem and finally get the IMFs without mode mixing. Then, the Hilbert transform is performed on the IMFs to obtain the amplitude, frequency and period of the IMFs. HHT has the following advantages: compared with Fourier transform, HHT can analyze nonlinear and non-stationary signals. Wavelet transform is essentially a Fourier transform with a flexible time-frequency window, so it also faces the limitations of Fourier transform, and the diversity of wavelet bases brings the problem about how to effectively select the wavelet bases. HHT has complete self-adaptability and is more advantageous in analyzing non-linear and non-stationary phenomena such as turbulence in the atmosphere. This is why this method is used in this article.

In the second section, we describe in detail the balloon sounding data and satellite observation data used, as well as our processing methods for these data. In the third section, we compare the SMLT retrieved from balloon sounding data with SMLT retrieved from satellite data. In the fourth section, we analyze the temporal and spatial distribution of SMLT. In the fifth section, we use HHT to extract and analyze the main modes and periods of SMLT altitude varying over time. The sixth section is our main conclusion.

## 2. Data and Data Processing Methods

### 2.1. Data

The balloon sounding data used for this paper was L band balloon sounding data detected twice a day (11:00 and 23:00) from Nanjing Sounding Station (113°05', 28°12') in 2015. The L band detection system is composed of GFE(L)-1 secondary wind measuring radar and GTS1 Radiosonde (a high altitude meteorological observation instrument). The main parameters of the detection are temperature, pressure, relative humidity, wind direction, wind speed and altitude. The average vertical resolution of the sounding balloon was about 9 m, and the average greatest detection altitude was about 28 km. The satellite data used in this article was wetPrf occultation data of COSMIC over nine years from the 1<sup>st</sup> day of 2007 to the 365<sup>th</sup> day of 2015 (data of 91 days was missing, from the 18<sup>th</sup> day of 2010 to the 212<sup>th</sup> day of 2010, from the 335<sup>th</sup> day of 2014 to the 364<sup>th</sup> day of 2014 and from the 27<sup>th</sup> day of 2015 to the 30<sup>th</sup> days of 2015). The COSMIC data version from the 1<sup>st</sup> day of 2007 to the 120<sup>th</sup> day of 2014 was named cosmic2013, and the COSMIC data version from the 121<sup>st</sup> day of 2014 to the 365<sup>th</sup> day of 2015 was named cosmic. The COSMIC data contains information on the temperature, pressure, water pressure and refractive index of the atmosphere over the ground to the altitude of 40 km with a resolution of 100 m.

### 2.2. Calculation of the Potential Temperature, Thorpe Scale $L_T$ and the Altitude and Thickness of SMLT

When processing balloon sounding data and satellite data, the potential temperature  $\theta$  was calculated via the temperature  $T$ , atmospheric pressure  $P$  and water vapor information. The water vapor information of the balloon sounding data is represented by relative humidity  $H$ , while the water vapor information of the satellite data is represented by vapor pressure  $e$ ; they can be transformed into

each other using a simple formula ( $H = \frac{e}{E_W} \times 100$ ,  $E_W$  is the saturated water vapor pressure). In this article, the calculation of  $\theta$  is based on Wilson et al. [29]:

$$\theta(i) = \theta(i - 1) \left[ 1 + N^2(i - 1) \frac{\Delta z}{g} \right]. \tag{3}$$

With air subsaturated,  $N^2 = \frac{g}{T} \left[ \left( \frac{\partial T}{\partial z} \right) + \Gamma_d \right]$ , where  $\Gamma_d$  is the dry adiabatic lapse rate; with air saturated,  $N^2 = \frac{g}{T} \left[ \left( \frac{\partial T}{\partial z} \right) + \Gamma_m \right] \left[ 1 + \frac{L_V q_s}{RT} \right] - \frac{g}{1+q_w} \left( \frac{dq_w}{dz} \right)$ , where  $L_V$  is the latent heat of vaporization of liquid water or ice.  $q_w = q_L + q_s$  is the total water mixing ratio. In our research we used the threshold value of relative humidity to determine if the air was saturated or not. The specific method is described by [30,31].

After obtaining and rearranging the  $\theta$  profiles, we could get Thorpe displacement  $D$ . For an independent inversion region, the sum of all  $D$  in its interior is zero. Since the noise of the instrument can cause false inversion, the method of Wilson et al. [22] was used to get rid of the fake inversion. The specific steps are to first calculate the variance of the noise with structure function [32]. After the change trend is removed, we get the structure function:

$$D(t') = \overline{[v(t+t') - v(t)]^2} = 2 \left[ \overline{V^2} - \overline{V(t+t')V(t)} + \overline{n^2} \right] = 2\overline{n^2} = 2\sigma_\theta^2 \tag{4}$$

$\sigma_\theta$  is the standard deviation of potential temperature noise. For an independent inversion area, if the change range of internal  $\theta$  is smaller than the change range of  $\theta$  caused by the noise, namely

$$W_\theta(n) < W_N^{99}(n)\sigma_\theta \tag{5}$$

then we take it as inversion caused by the noise and delete it.

The Thorpe scale  $L_T$  is obtained by calculating the root-mean-square of all the  $D$  in the inversion. In inverted regions of the free atmosphere, we define that the largest inversion area of  $L_T$  is the SMLT, and the altitude corresponding to its central position is considered to be the altitude of the SMLT, and the altitude difference between the upper and lower boundary is the thickness of the SMLT.

### 2.3. Calculation of the Fluctuation Period and Amplitude

In this article, we used HHT to calculate the period and amplitude [27]. HHT is divided into EMD and Hilbert transform. The steps for HHT are

(1) Supposing the original sequence is  $X(t)$ , find all of its local maximum and get upper envelope curves  $e_{\max}(t)$  with interpolation. The lower envelope curves  $e_{\min}(t)$  can be obtained in a similar way. We can get the mean envelope curves  $m_1(t) = \frac{[e_{\max}(t) + e_{\min}(t)]}{2}$  and further get the first component  $h_1(t)$ ,

$$h_1(t) = X(t) - m_1(t) \tag{6}$$

(2) Take  $h_1(t)$  as original sequence, repeat (1) k times until the standard deviation of two neighboring components satisfy the condition that  $0.2 < D_s < 0.3$ , where

$$D_s = \sum_{t=0}^T \left[ \frac{|h_{1(k-1)}(t) - h_{1k}(t)|^2}{h_{1(k-1)}^2(t)} \right] \tag{7}$$

$$h_{1k}(t) = h_{1(k-1)}(t) - m_{1k}(t) \tag{8}$$

At this time,  $h_{1k}(t)$  is IMF1, written  $c_1(t)$ .

(3) Repeat (1) and (2) until no IMF can be drawn.

Due to the scale mixing of EMD, EEMD is proposed based on EMD by Wu et al. [28]. The procedure is to add white noise on the original sequence and then perform EMD. Generally, the signal-to-noise ratio of white noise and original signal is 0.2–0.3 (0.2 is used in this article). Repeat the

previous two steps and average the results and get the final IMFs and a residual item of the original sequence, written as

$$X(t) = \sum_{i=1}^n c_i(t) + r(t) \quad (9)$$

Perform the Hilbert–Huang transform on each  $c_i(t)$  and get  $\hat{c}_i(t)$ , namely

$$\hat{c}_i(t) = \frac{1}{\pi} P \int_{-\infty}^{\infty} \frac{c_i(\tau)}{t - \tau} d\tau \quad (10)$$

so that we can further get instantaneous amplitude  $A_i(t)$  and instantaneous frequency  $\omega_i(t)$ ,

$$A_i(t) = \sqrt{c_i^2(t) + \hat{c}_i^2(t)} \quad (11)$$

$$\omega_i(t) = \frac{d \left\{ \arctan \left[ \frac{\hat{c}_i(t)}{c_i(t)} \right] \right\}}{dt} \quad (12)$$

By calculating the respect mean value of  $A_i(t)$  and  $\omega_i(t)$ , we could get the average amplitude, average frequency and average period.

### 3. Comparison of Inversion Results of Two Types of Data

In order to verify the results of satellite data, we compared the inversion results of balloon data detected twice a day in the Nanjing Sounding Station with that of the COSMIC data detected in the range of  $10^\circ \times 10^\circ$  centered with the Nanjing Radiosonde Station, from the 10<sup>th</sup> day to the 260<sup>th</sup> day of 2015 after eliminating the dates when data was missing. The elimination method is that if one kind of data is missing on a certain day, another kind of data of that day also needs to be eliminated. The  $L_T$ , altitude and thickness of SMLT are given a daily average. a, b and c in Figure 1 respectively show the anomalies of SMLT's  $L_T$ , altitude and thickness obtained from sounding data and COSMIC data (hereafter referred to as "two sorts of data"). For better observation, the sliding average of 30 days was carried out. Table 1 shows the statistical characteristics of  $L_T$ , altitude and thickness obtained from the two sorts of data. It can be seen from the figure and the table that the  $L_T$  and thickness values obtained by the COSMIC data were larger while the altitude values were smaller; however, in terms of  $L_T$ , altitude and thickness, the overall trends of the two sorts of data approximately coincided, and the statistical characteristics corresponded well. The difference between the average value of  $L_T$  and that of the thickness (COSMIC data - balloon data) is 256 m and 165 m respectively, about 2–3 times the resolution difference (about 90 m) of two sorts of data. We believed that the main reason for this difference is caused by the difference in resolution. For COSMIC data, lower resolution will lead to larger  $D$ . At the same time, lower resolution may cause Thorpe analysis to fail to accurately identify the upper and lower boundaries of the mixed layer and may even identify multiple mixed layers of similar altitudes as one layer, so that the thickness inversion results are larger. Difference in the mean altitude (COSMIC data - balloon data) was  $-1.33$  km. We believed that this difference is mainly caused by the difference in the space range of the two detections. First, the area that the sounding balloon can detect is very limited, only to the range of tens of kilometers around the sounding station, while for COSMIC data, in order to ensure occultation events occurring in our selected area at least once a day, we chose a larger area of  $10^\circ \times 10^\circ$ . The sporadicity and abruptness of the turbulence together caused the difference between the COSMIC data and balloon data inversion results. However, the correlation coefficients of  $L_T$ , altitude and thickness obtained by the two sorts of data were 0.57, 0.56 and 0.63 respectively, indicating that there was a moderate correlation between the two data. In general, although there were some differences in the inversion results of the two data, COSMIC could still retrieve the basic trend and the detailed characteristics of the SMLT changes. So, we thought that

the COSMIC data could meet the requirement to determine the basic characteristics of the SMLT. Based on this, the following study was conducted.

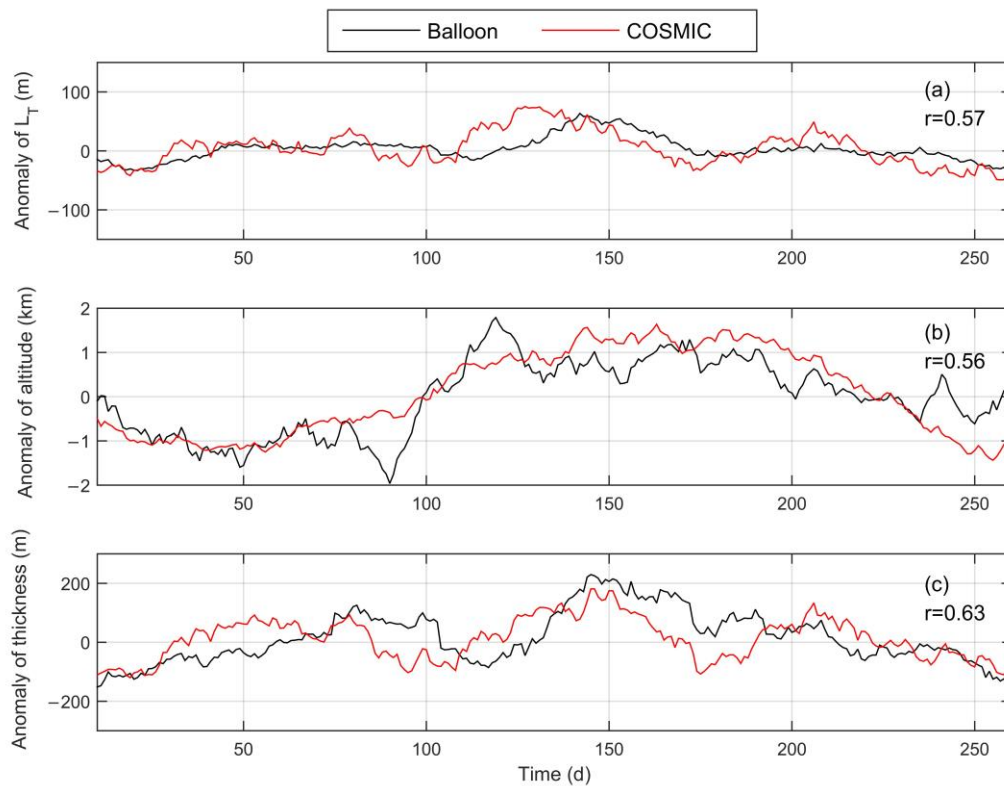


**Figure 1.** Anomalies of  $L_T$  (a), altitude (b) and thickness (c) obtained from the two sorts of data respectively.

**Table 1.** Comparison of statistical characteristics of  $L_T$ , altitude and thickness obtained from the two sorts of data.

	$L_T$ (m)	Altitude (km)	Thickness (m)
mean value of COSMIC	468	7.73	940
mean value of balloon	221	9.06	775
difference of the mean value	256	-1.33	165
Correlation coefficient	0.57	0.56	0.63

#### 4. The Temporal and Spatial Distribution of SMLT

In order to get the temporal and spatial distribution of SMLT from COSMIC data, we first obtained the data of nine years (from the first day of 2007 to the 365<sup>th</sup> day of 2015) in the range of 70° N–70° S. Then we processed each profile using the Thorpe analysis, reversed the altitude, thickness and  $L_T$  of SMLT and then averaged the inversion results in each 5° × 5° region as the result of the inversion of the center of the grid.

In order to reflect the characteristics of the SMLT varying according to the season, we performed a seasonal average of the SMLT in this section. Figure 2 shows the oblique and top views of the spatial distribution of SMLT in spring 2007. Since the influence of the sun in spring was relatively equal on the northern and southern hemispheres, the SMLT distribution around the equator was roughly symmetric. We could see from the oblique view that the altitude of SMLT clearly presented a bigger value in the tropical area, rapid dropping down in mid latitudes and a smaller value in high latitudes. However, the highest part of SMLT was not located at the equator, but in the area of 10–20° N and 10–20° S, and the maximum was over 10 km. The altitude in equatorial region was slightly lower, about 9.5 km. The

lowest altitude appeared in the area with a latitude larger than 50°, about 6 km. From the top view, we could see that the largest  $L_T$  was between 50° S and 50° N.  $L_T$  was approximately greater than 350 m, and some regions were even larger than 450 m. In the tropics,  $L_T$  was smaller in most high-SMLT regions; in regions where latitude was higher than 50°,  $L_T$  was the smallest, approximately less than 350 m.

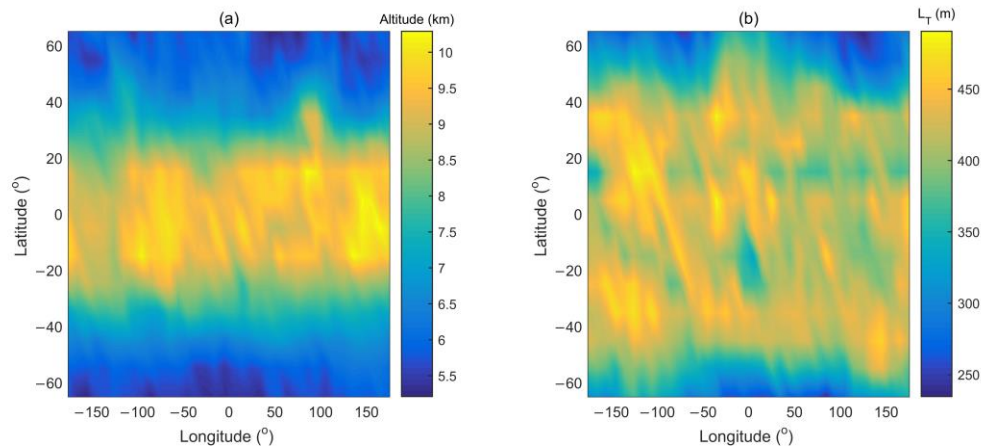


**Figure 2.** Altitude (a) and  $L_T$  (b) of the strongest mixed layer of the troposphere (SMLT) spatial distribution in Spring 2007.

In order to more clearly reflect the change in the altitude, thickness and  $L_T$  of SMLT with seasons, we carried out meridional and zonal averages of these three physical quantities respectively. Figure 3 shows the distribution of SMLT with longitude in spring, summer, autumn and winter after meridional averaging. Table 2 shows the statistical characteristics of Figure 3. As can be seen from Figure 3 and Table 2, the SMLT altitude generally fell between 7 and 8 km, with the annual average value 7.51 km and greater altitude in the summer. In the area of 80–100° E, there was always an obvious prominence in the four seasons with an altitude of about 8 km. This happened to be the longitude of the Tibetan Plateau, indicating that the large scale topography function of Tibetan Plateau had an impact on the altitude of SMLT. The thickness of SMLT was mostly between 700 and 900 m, with an average annual value of 804 m. The  $L_T$  of SMLT was mostly between 350 and 450 m with an annual average of 401 m. Similar to the altitude, the thickness and  $L_T$  of SMLT also show the characteristics of a larger value in summer.

**Table 2.** Statistical characteristics of SMLT of 2007 after meridional averaging.

	Altitude (km)			Thickness (m)			$L_T$ (m)		
	Maximum	Minimum	Average	Maximum	Minimum	Average	Maximum	Minimum	Average
spring	7.99	7.22	7.51	867	739	798	426	377	399
summer	8.29	7.21	7.57	872	754	817	421	382	406
autumn	8.03	7.17	7.50	862	736	799	425	375	399
winter	7.94	7.22	7.45	891	712	800	431	363	399
average	8.06	7.20	7.51	873	735	804	426	374	401

Figure 4 shows the distribution of SMLT with a latitude in spring, summer, autumn and winter after zonal averaging. Table 3 shows the statistical characteristics of Figure 4. From Table 3, we can see that the range of three physical quantities of the SMLT after the zonal averaging was larger than that after meridional averaging, and approximately 5.5–9.5 km, 538–591 m and 283–440 m, respectively. From Figure 4, we can see that, as analyzed in Figure 2, there were significant latitudinal differences in the altitude of SMLT, with the highest altitudes in the tropical region, slightly lower in the equatorial region, a rapid decline in the mid-latitude region and the lowest in the high latitudes. There was a clear seasonal variation of the zonal average distribution of SMLT, with a minor change in the southern hemisphere and the major change in the northern hemisphere. Especially in the section of 20–40° N,

the altitude of SMLT in summer and autumn was greater than that in spring and winter, making a smoother change of the SMLT altitude in the northern hemisphere in summer and autumn. In spring and winter, the maximum value of  $L_T$  in the northern hemisphere appears between 20° and 30° N, while in summer and autumn it moved northward to 40° N.

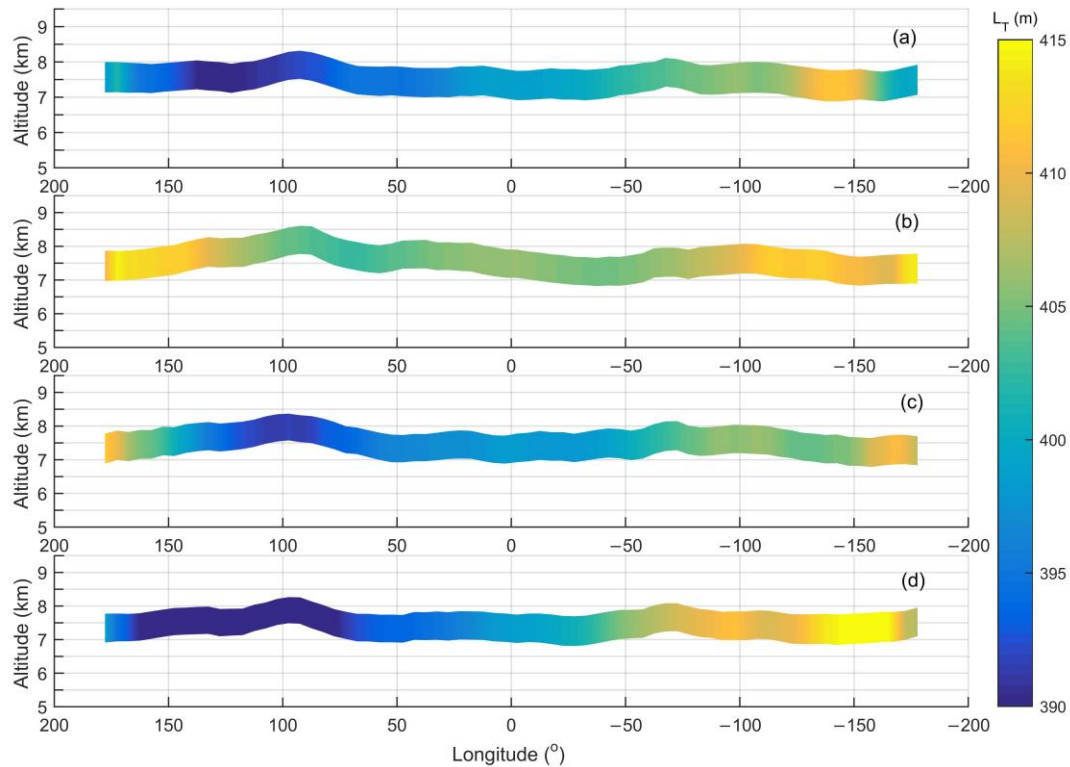


**Figure 3.** The distribution of SMLT of 2007 with a longitude after meridional averaging. (a), (b), (c) and (d) represent spring, summer, autumn and winter. The vertical thickness of the line represent thickness of SMLT, and the color of the line represent  $L_T$  of SMLT.

**Table 3.** Statistical characteristics of SMLT after zonal averaging in 2007.

	Altitude (km)			Thickness (m)			$L_T$ (m)		
	Maximum	Minimum	Average	Maximum	Minimum	Average	Maximum	Minimum	Average
spring	9.59	5.57	7.52	895	540	789	444	287	394
summer	9.77	5.65	7.65	882	554	812	436	287	404
autumn	9.45	5.63	7.57	884	515	793	439	276	396
winter	9.45	5.43	7.46	901	541	789	443	284	394
average	9.57	5.57	7.55	891	538	796	440	283	397

Based on the phenomena observed above, we believed that the fundamental reasons for the variation of SMLT were the seasonal variation of solar radiation and the difference in the topography of the northern and southern hemispheres. Since the subsolar point always moves between the Tropic of Capricorn and the Tropic of Cancer, the altitude of the SMLT in the low-latitude regions was always greater than in the mid-latitudes. In the southern hemisphere, the land area is smaller and mainly distributed in the lower latitudes, so the land area of the southern hemisphere affected by the sun did not change much in the course of the movement of the sun. In the northern hemisphere, the land area in low latitudes accounts for only a small part of the total land area, so the land area of the northern hemisphere affected by the sun would gradually become larger in the course of the northward movement of the subsolar point. In addition, the large-scale topography of the Qinghai–Tibet Plateau, the Rocky Mountains and the Iranian Plateau in the region of 30–60° N contribute to the uplifting of the boundary layer top and tropopause in these regions. When the heights of the boundary layer

top and tropopause rise, it will cause the updraft of wind speed maximum area in the middle of the troposphere, and the wind shear and gravity waves are the main causes of turbulence [33,34], so the SMLT will also rise. During the southward shift of the subsolar point, the influence of the sun on the 30–60° N region weakened, so the altitude of the SMLT also gradually decreased.

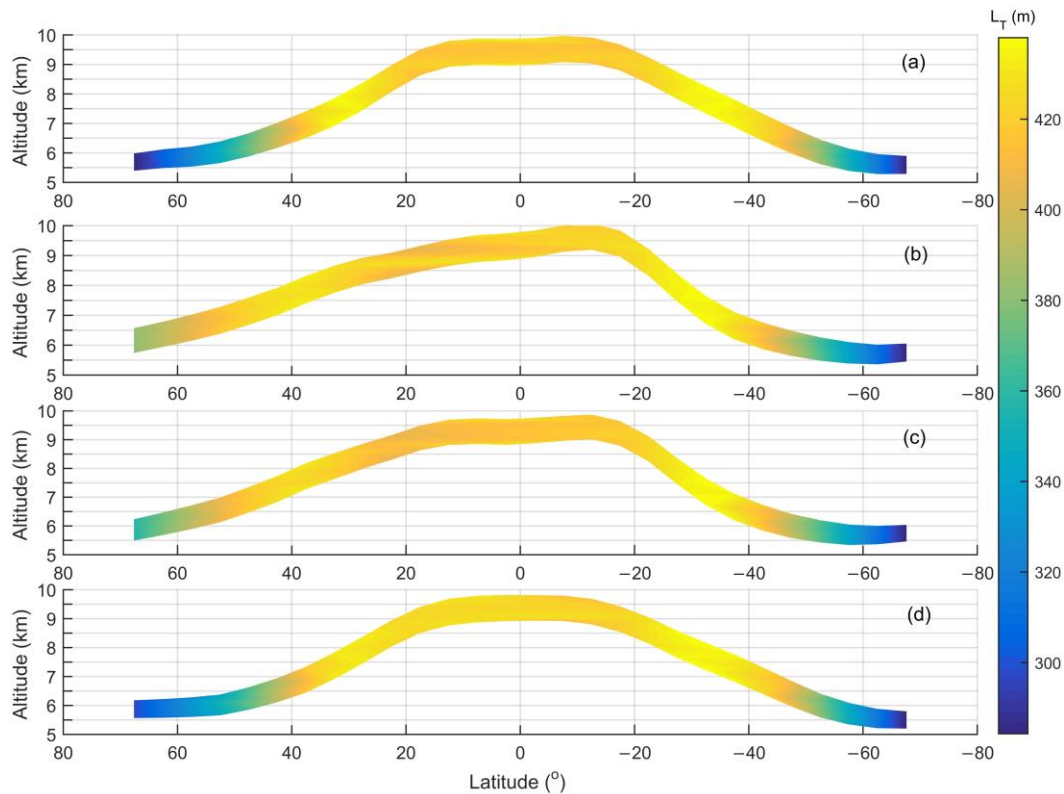


**Figure 4.** The distribution of SMLT with a latitude after zonal averaging in 2007. (a), (b), (c) and (d) represent spring, summer, autumn and winter. The vertical thickness of the line represents thickness of SMLT, and the color of the line represents  $L_T$  of SMLT.

## 5. HHT of SMLT Altitude over Time

Through the previous analysis, we found that the change of the zonal average SMLT altitude was more obvious with season. In order to have more detailed research on the characteristics of the variation of zonal average SMLT altitude (hereafter abbreviated as "altitude variation"), we used the HHT method. First, we selected the altitude variation of 45° N as the research object. As shown in Figure 5, the SMLT altitude at 45° N was within the altitude range of 6–7.8 km, with an average of about 6.76 km, showing an obvious annual period fluctuation, on which the small but acute fluctuation was superimposed. In order to be able to identify other periodic fluctuations besides annual fluctuations, we performed HHT processing for altitude vibrations at 45° N and obtained the average frequency, average period and average amplitude of IMFs (hereafter abbreviated as "frequency", "period" and "amplitude"). The decomposition results are shown in Figure 6 and Table 4. After EEMD, altitude variation could be divided into 10 IMFs and one residual item. From IMF1 to IMF10, the curve gradually became smooth, the frequency gradually decreased from 0.3106 to 0.0003 Hz, and the period increased from 3 to 3320 days. In the 10 IMF, we focused only on the IMF of the period more than half a year and the period less than 4.5 years (we had only 9 years of data), that is, IMF6, IMF7 and IMF8. The IMF with the largest amplitude was IMF6, its amplitude was 535 m and its corresponding period was 358 days. Next was IMF7, the amplitude was 90 days and the corresponding period was 442 days. The minimum amplitude was IMF8, the amplitude was only 29 m and the average period

was 1510 days, which is about four years. In general, at 45° N, the fluctuation of the annual period of the altitude variation was most prominent, but there were still other small amplitude fluctuations.

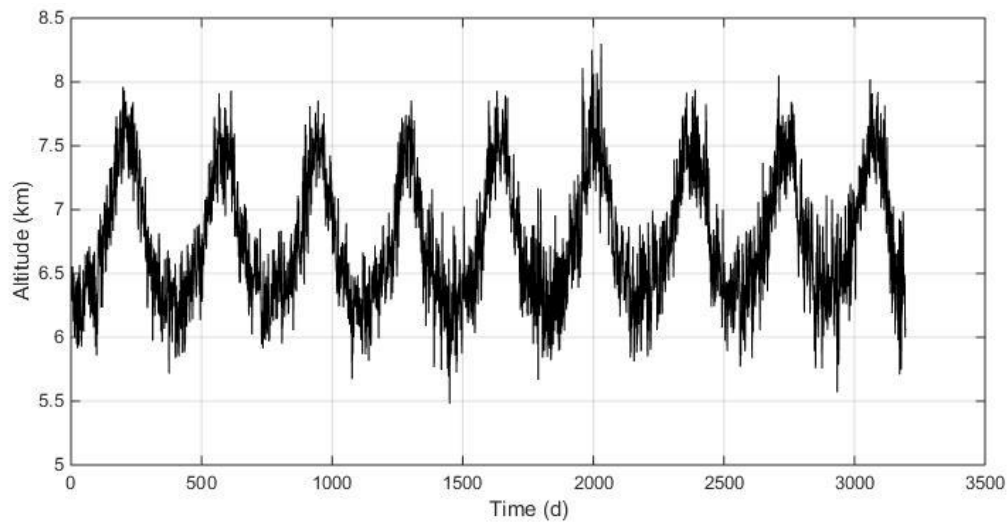


Figure 5. Altitude variation at 45° N from 2007 to 2015.

Table 4. Characteristics of intrinsic mode functions (IMFs) obtained from Hilbert–Huang transform (HHT) of altitude variation at 45° N.

IMF	IMF1	IMF2	IMF3	IMF4	IMF5	IMF6	IMF7	IMF8	IMF9	IMF10
frequency (Hz)	0.3105	0.1393	0.0658	0.0286	0.0116	0.0028	0.0024	0.0007	0.0004	0.0003
period (d)	3	7	15	35	86	358	422	1510	2551	3320
amplitude (m)	11	8	10	20	75	535	90	29	38	1

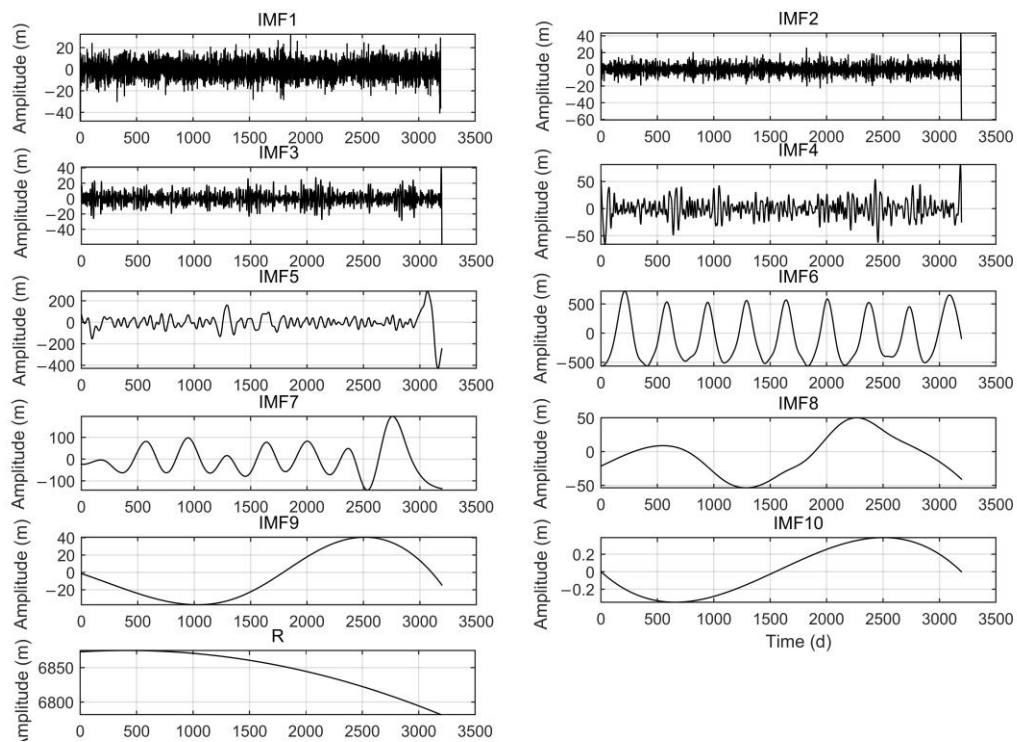
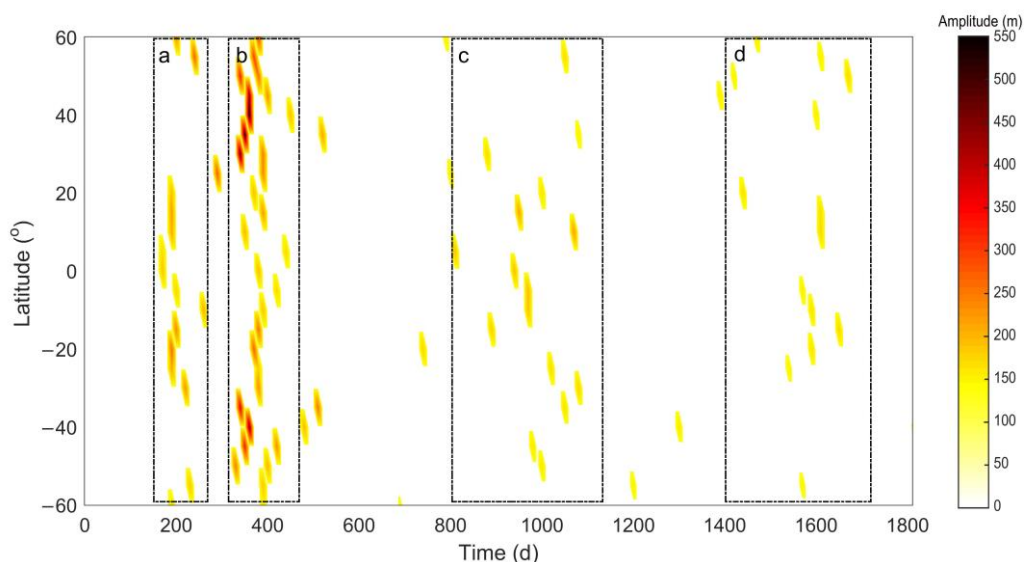


Figure 6. The result of ensemble empirical mode decomposition (EEMD) of altitude variation at 45° N from 2007 to 2015.

Each point in the Figure 7 represents an IMF, and the ordinate of each point represents the latitude of the IMF, the abscissa represents the period of the IMF and the color represents the amplitude of the IMF. We could roughly divide the image into four main areas as follows: a, b, c and d. In area a, the points mainly located in the low latitude region, the corresponding period is about half a year and the amplitude is between 50 and 250 m; the amplitude of the IMF in the low latitudes of the southern hemisphere (50–150 m) was larger than that in the low latitudes of the northern hemisphere (100–250 m). In the middle latitudes near 40° S and 40° N, there was basically no IMF with a period of about half a year. The period corresponding to the area b was mainly between 300 d and 400 d, which is about one year. In contrast to area a, the IMFs with the larger amplitude in the area b were mainly located in the middle latitudes, the amplitudes in the mid latitudes in the northern hemisphere were the largest and could reach 550 m, and the amplitudes in the mid latitudes in the southern hemisphere were slightly lower, with the maximum amplitude being 471 m. In the low latitude of area b, the amplitude of IMFs was between 100 and 200 m, and like area a, the amplitude in the southern hemisphere was large. Moreover, the points in area c and area d were sparse, and their corresponding periods were about 3 years and 4 years respectively, with amplitudes between 50–150 m.



**Figure 7.** The result of HHT of altitude variation of 70° S–70° N from 2007 to 2015.

From the previous analysis, we could see that for the area a and b, the points in the northern and southern hemispheres were mostly symmetrical; IMFs with a period of approximately half a year and a period of approximately one year could be simultaneously extracted from altitude variation in low latitudes. In the mid-latitude region, only the IMFs with a period of about one year could be extracted and the amplitude was larger. This indicates that the altitude change was affected by the solar radiation, because in the course of the movement of the sun, the mid latitudes could not be radiated directly, and the influence of the sun on the middle latitudes was also changing in a year period, so the SMLT in the middle latitudes will show a fluctuation period of half a year. In the low latitudes between the Tropic of Capricorn and the Tropic of Cancer, the sunlight shines vertically once every half a year in average, so the SMLT in the middle latitudes will be characterized by a half year period. In addition, the amplitude of low latitude modes was larger in the southern hemisphere, while the amplitude of mid latitude modes was larger in the northern hemisphere, reflecting the role of topographic differences between the northern and southern hemispheres in altitude variation. This was consistent with our analysis in the last paragraph of the previous section.

## 6. Conclusions

This article first proposed the concept of the strongest mixed layer in the troposphere. Based on this, the sounding data was used to analyze the ability of COSMIC data to determine the characteristics of the SMLT. We found that the results obtained by the two sorts of data had good consistency, so we thought that COSMIC data could be used to determine the SMLT altitude value, and to evaluate the basic change trend of thickness and  $L_T$  of the SMLT. Therefore, we then used the COSMIC data to invert the global spatio-temporal distribution of the SMLT from 2007 to 2015, and analyzed the distribution characteristics of SMLT in spring, summer, autumn and winter in 2007. We found that SMLT generally shows the maximum altitude at the low latitudes, a rapid decline at the mid-latitudes and the minimum altitude at the high latitudes, and it was influenced by the large scale topography. At the same time, the altitude of the SMLT varied with the season, especially in the mid-latitudes. This indicates that the variation of SMLT altitude was affected by both the topography and solar radiation.

The above research brought us new discoveries and also brought us many problems. First, the low resolution of the COSMIC data limited the accuracy of  $L_T$  and thickness calculations. Therefore, if we want to carry out further research, we need higher resolution and higher precision detection data. Second, the derivation of the conclusion that the variation of SMLT altitude was affected by the dual effects of topography and solar radiation was relatively rough, the mechanism of their interaction needs further study, and we will improve the research on this aspect in the next work. Third, the fluctuation of the SMLT altitude with a period of about half a year and a period of about one year can be explained by the movement of the subsolar point, but we have not found a reasonable explanation for the fluctuation with a period of 3 years and 4 years, and this will also be a focal point of our future work.

**Author Contributions:** Data curation, Z.S., L.Z. and Y.H.; Formal analysis, Z.S., L.Z. and Y.H.; Investigation, Y.H.; Methodology, Z.S., L.Z. and Y.H.; Writing – original draft, Z.S. and L.Z. All authors have read and agreed to the published version of the manuscript.

**Funding:** The study was partly supported by the National Natural Science Foundation of China (Grant No. 41875045, 41775039) and the National Key Research and Development Project, China (Grant No. 2018YFC1506200).

**Acknowledgments:** The authors acknowledge the COSMIC Data Analysis and Archive Center (CDAAC) for provision of the COSMIC GPS RO soundings.

**Conflicts of Interest:** The authors declare no conflict of interest.

## References

1. Theuerkauf, A.; Gerding, M.; Lübken, F.J. LITOS—A new balloon-borne instrument for fine-scale turbulence soundings in the stratosphere. *Atmos. Meas.* **2011**, *4*, 3455–3487. [[CrossRef](#)]
2. Zhang, J.; Tian, W.; Xie, F.; Chipperfield, M.P.; Feng, W.; Son, S.W.; Abraham, N.L.; Archibald, A.T.; Bekki, S.; Butchart, N.; et al. Stratospheric ozone loss over the Eurasian continent induced by the polar vortex shift. *Nat. Commun.* **2018**, *9*, 1–8. [[CrossRef](#)] [[PubMed](#)]
3. Alisse, J.; Sidi, C. Experimental probability density functions of small-scale fluctuations in the stably stratified atmosphere. *J. Fluid Mech.* **2000**, *402*, 137–162. [[CrossRef](#)]
4. Sheng, Z.; Jiang, Y.; Wan, L.; Fan, Z.Q. A study of atmospheric temperature and wind profiles obtained from rocketsondes in the chinese midlatitude region. *J. Atmos. Ocean. Technol.* **2015**, *32*, 722–735. [[CrossRef](#)]
5. Wang, W.; Shanguan, M.; Tian, W.; Schmidt, T.; Ding, A. Large uncertainties in estimation of tropical tropopause temperature variabilities due to model vertical resolution. *Geophys. Res. Lett.* **2019**, *46*, 10043–10052. [[CrossRef](#)]
6. Zhao, X.R.; Sheng, Z.; Li, J.W.; Yu, H.; Wei, K.J. Determination of the “wave turbopause” using a numerical differentiation method. *J. Geophys. Res. Atmos.* **2019**, *124*, 10592–10607. [[CrossRef](#)]
7. Clayson, C.A.; Kantha, L. On Turbulence and Mixing in the Free Atmosphere Inferred from High-Resolution Soundings. *J. Atmos. Ocean. Technol.* **2008**, *25*, 833–852. [[CrossRef](#)]
8. Chang, S.; Sheng, Z.; Du, H.; Ge, W.; Zhang, W. A channel selection method for hyperspectral atmospheric infrared sounders based on layering. *Atmos. Meas. Tech.* **2020**, *13*, 629–644. [[CrossRef](#)]

9. Xie, F.; Li, J.; Zhang, J.; Tian, W.; Hu, Y.; Zhao, S.; Sun, C.; Ding, R.; Feng, J.; Yang, Y. Variations in north Pacific sea surface temperature caused by Arctic stratospheric ozone anomalies. *Environ. Res. Lett.* **2017**, *12*, 114023. [[CrossRef](#)]
10. He, Y.; Sheng, Z.; He, M. Spectral Analysis of Gravity Waves from Near Space High-Resolution Balloon Data in Northwest China. *Atmosphere* **2020**, *11*, 133. [[CrossRef](#)]
11. He, Y.; Sheng, Z.; He, M. The First Observation of Turbulence in Northwestern China by a Near-Space High-Resolution Balloon Sensor. *Sensors* **2020**, *20*, 677. [[CrossRef](#)] [[PubMed](#)]
12. Cohn, S.A. Radar measurements of turbulent eddy dissipation rate in the troposphere: A comparison of techniques. *J. Atmos. Ocean. Technol.* **1995**, *12*, 85–95. [[CrossRef](#)]
13. Hooper, D.A.; Thomas, L. Complementary criteria for identifying regions of intense atmospheric turbulence using lower VHF radar. *J. Atmos. Sol. Terr. Phys.* **1998**, *60*, 49–61. [[CrossRef](#)]
14. Thorpe, S.A. Turbulence and mixing in a Scottish Loch. *Philos. Trans. Roy. Soc. London* **1977**, *286*, 125–181.
15. Thorpe, S.A. *The Turbulent Ocean*; Cambridge University Press: Cambridge, UK, 2005; 439p.
16. Balsley, B.B.; Kantha, L.; Colgan, W. On the Use of Slow Ascent Meter-Scale Sampling (SAMS) Radiosondes for Observing Overturning Events in the Free Atmosphere. *J. Atmos. Ocean. Technol.* **2009**, *27*, 766–775. [[CrossRef](#)]
17. Nath, D.; Ratnam, M.V.; Patra, A.K.; Murthy, B.V.K.; Rao, S.V.B. Turbulence characteristics over tropical station Gadanki (13.5°N, 79.2°E) estimated using high-resolution GPS radiosonde data. *J. Geophys. Res. Atmos.* **2010**, *115*, D07102.
18. Kantha, L.; Hocking, W. Dissipation rates of turbulence kinetic energy in the free atmosphere: MST radar and radiosondes. *J. Atmos. Sol. -Terr. Phys.* **2010**, *73*, 1043–1051. [[CrossRef](#)]
19. Wilson, R.; Dalaudier, F.; Luce, H. Can one detect small-scale turbulence from standard meteorological radiosondes? *Atmos. Meas. Tech.* **2012**, *4*, 795–804. [[CrossRef](#)]
20. Muhsin, M.; Sunilkumar, S.V.; Ratnam, M.V.; Parameswaran, K.; Murthy, B.V.K.; Ramkumar, G.; Rajeev, K. Diurnal variation of atmospheric stability and turbulence during different seasons in the troposphere and lower stratosphere derived from simultaneous radiosonde observations at two tropical stations, in the Indian Peninsula. *Atmos. Res.* **2016**, *180*, 12–23. [[CrossRef](#)]
21. Luce, H.; Fukao, S.; Dalaudier, F.; Crochet, M. Strong Mixing Events Observed near the Tropopause with the MU Radar and High-Resolution Balloon Techniques. *J. Atmos. Sci.* **2002**, *59*, 2885–2896. [[CrossRef](#)]
22. Wilson, R.; Luce, H.; Dalaudier, F.; Lefrère, J. Turbulence Patch Identification in Potential Density or Temperature Profiles. *J. Atmos. Ocean. Technol.* **2010**, *27*, 977–993. [[CrossRef](#)]
23. Hwang, C.; Tseng, T.P.; Lin, T.; Svehla, D.; Schreiner, B. Precise orbit determination for the formosat-3/cosmic satellite mission using gps. *J. Geod.* **2009**, *83*, 477–489. [[CrossRef](#)]
24. Kuo, Y.H.; Sokolovskiy, S.; Anthes, R.; Andenberghe, F.V. Assimilation of gps radio occultation data for numerical weather prediction. *Terr. Atmos. Ocean. Sci.* **2010**, *11*, 157–186. [[CrossRef](#)]
25. Rocken, C. Cosmic system description. *Terr. Atmos. Ocean. Sci.* **2011**, *11*, 21–52. [[CrossRef](#)]
26. Fan, Z.Q.; Sheng, Z.; Shi, H.Q.; Yi, X.; Jiang, Y.; Zhu, E.Z. Comparative assessment of cosmic radio occultation data and timed/saber satellite data over china. *J. Appl. Meteorol. Climatol.* **2014**, *54*, 1931–1943. [[CrossRef](#)]
27. Huang, N.E.; Shen, Z.; Long, S.R.; Wu, M.C.; Shih, H.H.; Zheng, Q.; Yen, N.C.; Tung, C.C.; Liu, H.H. The empirical mode decomposition and the hilbert spectrum for nonlinear and non-stationary time series analysis. *Proc. Math. Phys. Eng. Sci.* **1998**, *454*, 903–995. [[CrossRef](#)]
28. Wu, Z.; Huang, N.E. Ensemble empirical mode decomposition: A noise-assisted data analysis method. *Adv. Adapt. Data Anal.* **2009**, *1*, 1–41. [[CrossRef](#)]
29. Wilson, R.; Luce, H.; Hashiguchi, H.; Shiotani, M. On the effect of moisture on the detection of tropospheric turbulence from in situ measurements. *Atmos. Meas. Tech.* **2013**, *6*, 697–702. [[CrossRef](#)]
30. Poore, K.D.; Wang, J.; Rossow, W.B. Cloud Layer Thicknesses from a Combination of Surface and Upper-Air Observations. *J. Clim.* **1995**, *8*, 550–568. [[CrossRef](#)]
31. Zhang, J.; Chen, H.; Li, Z.; Fan, X.; Peng, L.; Yu, Y.; Cribb, M. Analysis of cloud layer structure in Shouxian, China using RS92 radiosonde aided by 95 GHz cloud radar. *J. Geophys. Res. Atmos.* **2010**, *115*, D00K30. [[CrossRef](#)]
32. Gavrilov, N.M.; Luce, H.; Crochet, M.; Dalaudier, F.; Fukao, S. Turbulence parameter estimations from highresolution balloon temperature measurements of the MUTSI-2000 campaign. *Ann. Geophys.* **2005**, *23*, 2401–2413. [[CrossRef](#)]

33. Strelnikov, B.; Szewczyk, A.; Strelnikova, I.; Latteck, R.; Baumgarten, G.; Lübken, F.J.; Rapp, M.; Fasoulas, S.; Löhle, S.; Eberhart, M.; et al. Spatial and temporal variability in mlt turbulence inferred from in situ and ground-based observations during the wadis-1 sounding rocket campaign. *Ann. Geophys.* **2017**, *35*, 547–565. [[CrossRef](#)]
34. Xu, X.; Wang, Y.; Xue, M.; Zhu, K. Impacts of horizontal propagation of orographic gravity waves on the wave drag in the stratosphere and lower mesosphere. *J. Geophys. Res. Atmos.* **2017**, *122*, 11–301. [[CrossRef](#)]



© 2020 by the authors. Licensee MDPI, Basel, Switzerland. This article is an open access article distributed under the terms and conditions of the Creative Commons Attribution (CC BY) license (<http://creativecommons.org/licenses/by/4.0/>).